PHYSICS

Reconnection-driven energy cascade in magnetohydrodynamic turbulence

Chuanfei Dong[1,2]†*, Liang Wang[2,1]†, Yi-Min Huang[2,1], Luca Comisso[3], Timothy A. Sandstrom[4], Amitava Bhattacharjee[1,2]

Magnetohydrodynamic turbulence regulates the transfer of energy from large to small scales in many astrophysical systems, including the solar atmosphere. We perform three-dimensional magnetohydrodynamic simulations with unprecedentedly large magnetic Reynolds number to reveal how rapid reconnection of magnetic field lines changes the classical paradigm of the turbulent energy cascade. By breaking elongated current sheets into chains of small magnetic flux ropes (or plasmoids), magnetic reconnection leads to a previously undiscovered range of energy cascade, where the rate of energy transfer is controlled by the growth rate of the plasmoids. As a consequence, the turbulent energy spectra steepen and attain a spectral index of −2.2 that is accompanied by changes in the anisotropy of turbulence eddies. The omnipresence of plasmoids and their consequences on, for example, solar coronal heating, can be further explored with current and future spacecraft and telescopes.

INTRODUCTION

Understanding the transfer of energy in magnetohydrodynamic (MHD) turbulence is crucial for tackling many outstanding astrophysical problems, such as solar and stellar coronal heating, star formation, cosmic ray transport, and the interstellar medium evolution. For more than half a century, it has been widely accepted that the energy cascade in turbulent plasmas, such as the Sun's atmosphere, is controlled by MHD wave interactions (*1*–*3*). However, one essential feature of MHD turbulence is the ubiquitous presence of sheets of intense electric current (known as current sheets), which are preferential locations for rapid breaking and reconnection of magnetic field lines (*4*, *5*), a fundamental physical process in magnetized plasmas whereby stored magnetic energy is converted into heat and kinetic energy of charged particles. It is yet an open question whether magnetic reconnection can substantially change the transfer of energy from large to small scales in a wide variety of astrophysical systems.

One of the most common approaches to investigating the effect of a physical process on the turbulent energy cascade is to study the associated energy spectra. It has been widely observed by different spacecraft and telescopes that turbulent energy spectra can break at either viscoresistive or kinetic scales (*6*–*8*). Recent analytic studies suggest that magnetic reconnection may also break the turbulent energy spectra and thus create a newly identified range of energy transfer when the growth time scale of the magnetic flux ropes (or plasmoids), $1/\gamma_p$, becomes much shorter than the nonlinear eddy turnover time, τ_{nl} (*9*–*13*). Plasmoids develop in intense and elongated current sheets undergoing reconnection, and in MHD turbulence, the spatial scales and aspect ratios of those current sheets are controlled by the magnetic Reynolds number, R_m, which quantifies the relative magnitudes of plasma convection and resistive diffusion. At sufficiently large R_m ($>10^5$), as in the solar atmosphere, magnetic reconnection is expected to be a ubiquitous phenomenon, as the thinning of current sheets can lead to a copious formation of plasmoids via the tearing instability (*14*–*18*), potentially changing the energy transfer across scales.

Because of the complex, nonlinear nature of the turbulent energy cascade, direct numerical simulations (DNSs) are likely the best means to investigate the role of magnetic reconnection in the energy transfer across scales and how it changes the turbulent energy spectra. To date, no evidence for the newly identified range of the turbulent energy cascade due to magnetic reconnection has been provided by DNSs in realistic three dimensions (3D) (*19*, *20*). Such DNSs are extremely challenging, mainly because of the high grid resolution required to capture the fine structure of the omnipresent current sheets in a turbulent plasma at large R_m. In addition, MHD turbulence and magnetic reconnection are known to behave differently in 2D and 3D (*19*, *21*); therefore, 3D DNSs with large R_m are essential to fundamentally address this question.

RESULTS

Here, we present the world's largest 3D MHD turbulence simulation, at a cost of ~200 million Central Processing Unit (CPU) hours, that self-consistently produces myriad fine current sheets. An elongated ($1 \times 1 \times 2$) periodic box with ~$10{,}000 \times 10{,}000 \times 5000$ grid cells was adopted to resolve the thin current sheets that develop at large R_m ($= 10^6$) [and the effective R_m ($R_{m,\mathrm{eff}}$) $= 2 \times 10^5$ based on the energy injection scale]. We initialized the simulations with uncorrelated, equipartitioned velocity and magnetic field fluctuations superimposed by a strong mean magnetic field in the elongated direction (see Materials and Methods for the detailed model setup). Such field configurations are common in a variety of astrophysical systems, such as solar/stellar coronae and the interstellar medium. Compared with earlier 3D MHD turbulence simulations, the most prominent development here is that the current study reaches an unprecedented high-R_m regime, such that the

[1]Princeton Plasma Physics Laboratory, Princeton University, Princeton, NJ 08540, USA. [2]Department of Astrophysical Sciences, Princeton University, Princeton, NJ 08544, USA. [3]Department of Astronomy and Columbia Astrophysics Laboratory, Columbia University, New York, NY 10027, USA. [4]NASA Ames Research Center, Mountain View, CA 94043, USA.
†These authors contributed equally to this work.
*Corresponding author. Email: dcfy@princeton.edu

ubiquitous reconnecting current sheets in a turbulent bath become unstable to the tearing instability.

The turbulent structures from our large-scale MHD simulation are visualized in Fig. 1. In Fig. 1A, volume rendering of the current density |**J**| depicts MHD turbulence in the entire simulation domain at the fully developed stage. Specifically, strong current sheets are ribbon-like (with large aspect ratios) and are aligned with the mean magnetic field B_{z0} due to the parallel coherence of perturbations. Meanwhile, they are also current sheets in the perpendicular plane aligned with in-plane perturbed magnetic fields. These ribbon-shaped current sheets are subject to the tearing instability during their dynamical evolution (see Fig. 1D) (*14*–*18*). The current density |**J**| in different *x*-*y* slices can be seen in movie S1. One of these current sheets undergoing magnetic reconnection is highlighted in a zoomed-in subdomain (Fig. 1, B and C), within which "ripples" induced by the formation of plasmoids/magnetic flux ropes are present on the current density isosurfaces. We cut a 2D slice across the embedded 3D magnetic flux ropes for J_z (Fig. 1C; also see Materials and Methods for a selected flux-rope bundle at different viewing angles). The current sheet in the subdomain

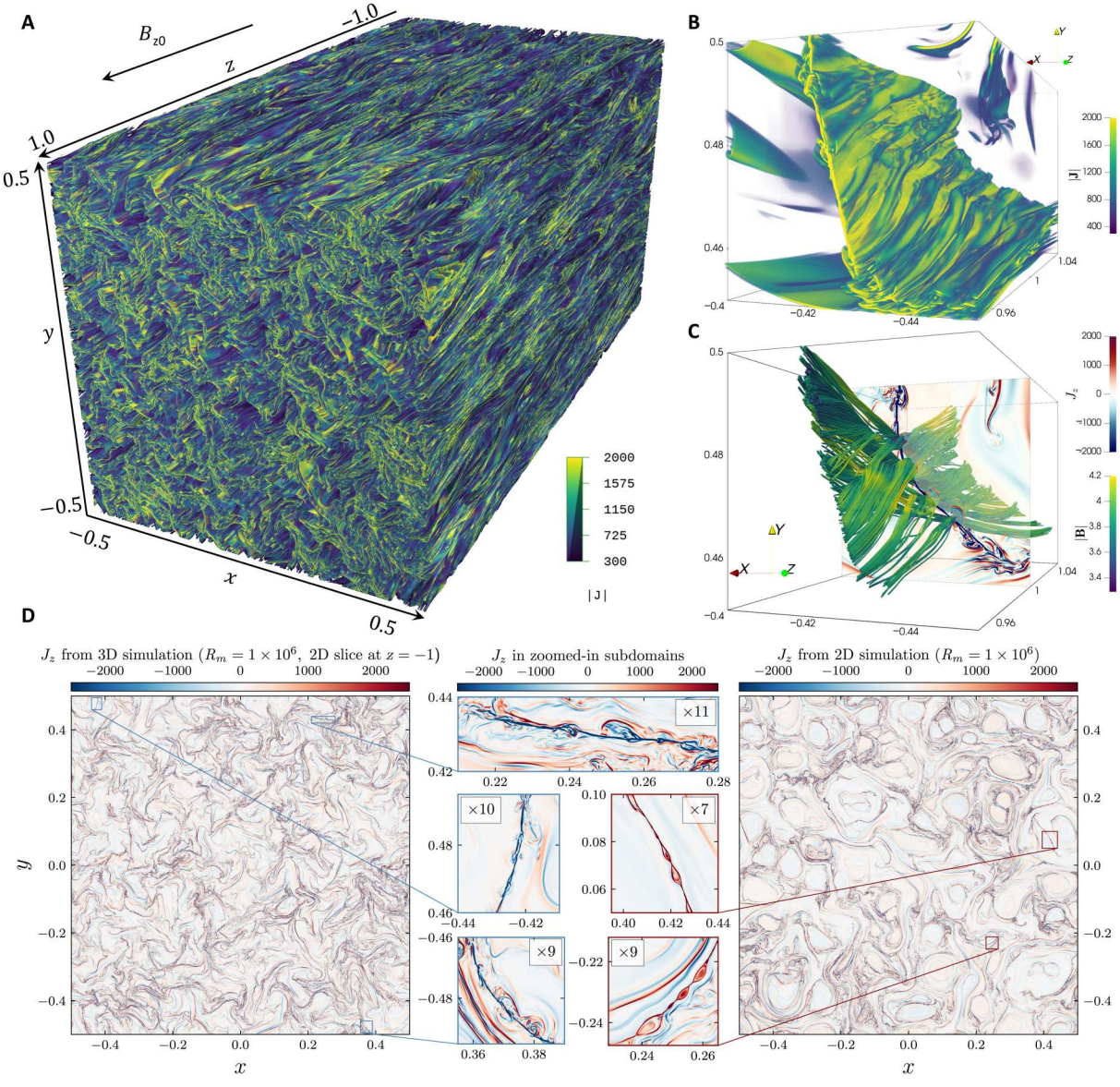

Fig. 1. Reconnecting current sheets and magnetic flux ropes in MHD turbulence. (**A**) Volume rendering of the current density |**J**| in the entire domain at a stage when turbulence is fully developed. Myriad of current sheets is evident in the plane perpendicular to the mean magnetic field B_{z0}. (**B**) and (**C**) depict one reconnecting current sheet and the embedded flux ropes in a small subdomain [within the boundaries (− 0.45, − 0.4) × (0.45, 0.5) × (0.95, 1.05)]. (B) shows the volume rendering of |**J**|, while (C) displays magnetic field lines (colored by |**B**|) associated with the featured current sheet (including magnetic flux ropes) and an *x*-*y* slice view of the current density component, J_z, along the mean magnetic field. (**D**) Out-of-plane current density J_z in an *x*-*y* slice (at $z = -1$) of the 3D turbulence simulation (left) compared with the corresponding result from a 2D simulation (right). Copious formation of magnetic flux ropes/plasmoids occurs in both 3D and 2D simulations despite the different morphology. Zoomed-in subdomains are used to illustrate the increased morphological complexity that characterizes the 3D simulation.

exhibits features similar to those observed in previous simulations of a single 3D reconnecting current layer (*19*, *22*, *23*). This subdomain (0.025% of the complete volume) is representative of the types of coherent structures that develop throughout the entire domain. Reconnection-produced magnetic flux ropes in 3D exhibit a more complex morphology than their 2D counterpart. This is illustrated in Fig. 1D, in which the out-of-plane current density, J_z, in one arbitrary x-y slice, points out that the reconnecting current sheet structures in 3D are fractured (or disrupted) and differ substantially from the island-like morphology in 2D (*22*–*26*) despite the similar size of the flux ropes.

Our simulation identifies a previously unexplored mechanism for energy transfer through the breakup of reconnecting current sheets into smaller fragments, which occurs generically in the large-R_m regime studied here (Fig. 1D). The role of reconnection in controlling the energy transfer is supported by its imprint on the energy spectrum of the turbulent cascade in Fig. 2. At large scales, $k_\perp \lesssim k_*$, both the magnetic energy spectrum $E_B(k_\perp)$ and the kinetic energy spectrum $E_U(k_\perp)$ follow a power law with a slope of −3/2 (see dashed fitted lines), in agreement with expectations for the inertial range of a strong turbulent cascade mediated by Alfvén waves when accounting for a reduction of nonlinearity due to dynamic alignment (*27*). At scales $k_* \lesssim k_\perp \lesssim k_\eta$, current sheets in this tearing-mediated regime (i.e., reconnection-driven regime, as highlighted by the shaded region in Fig. 2) exhibit numerous

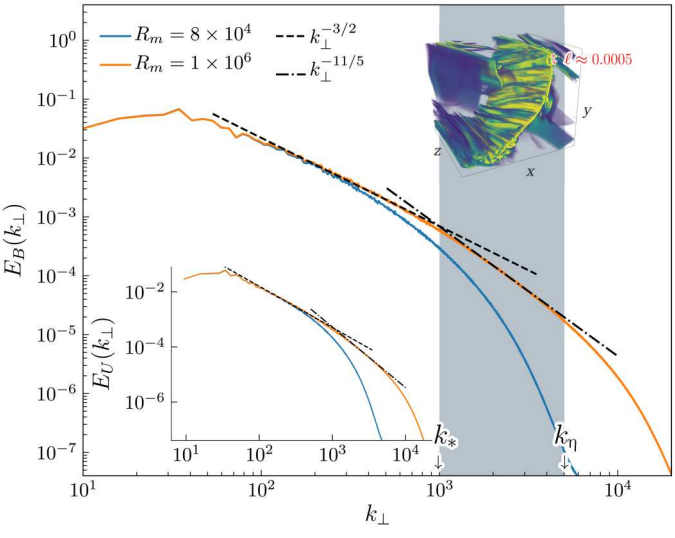

Fig. 2. Steepening of energy spectra in reconnection-driven energy cascade. Field perpendicular magnetic and kinetic energy spectra, $E_B(k_\perp)$ and $E_U(k_\perp)$, showing a standard inertial range with a slope $E_{B,U}(k_\perp) \propto k_\perp^{-3/2}$ and a reconnection-driven (or tearing-mediated) subinertial range with a slope $E_{B,U}(k_\perp) \propto k_\perp^{-11/5}$ for large R_m (orange curves). The subinertial range is absent in an equivalent 3D simulation with lower R_m (blue curves). The shaded area emphasizes the reconnection-driven subinertial range, with wave numbers corresponding to the typical transverse scales of the flux ropes shown in the inset. The left edge of the shaded range is identified at $k \approx 10^3 \approx R_{m,\mathrm{eff}}^{7/4}$, where $R_{m,\,\mathrm{eff}} \approx 2 \times 10^5$ is computed with the energy injection scale at $k \approx 30$. The right edge, marked by k_η, is the dissipation scale defined such that $\eta \int_0^{k_\eta} E_B(k_\perp) k_\perp^2 \mathrm{d}k_\perp$ accounts for approximately half of the resistive dissipation power $\eta\langle J^2\rangle$. The small volume rendering inset illustrates a typical reconnecting current layer, which is ubiquitous in this range, with the transverse size of an embedded flux rope annotated in red.

reconnecting structures, or magnetic flux ropes, as shown in the inset. As a result, flux rope formation through reconnection dominates over MHD wave interactions in controlling turbulent energy transfer. Consequently, the energy spectrum in this range (termed as subinertial range hereafter) becomes steeper and is characterized by a spectral index of −11/5 when R_m is sufficiently large, which is broadly consistent with the theoretical predictions (*9*–*12*). The turbulent energy spectrum breaks at $k_* \approx 1000$ in Fig. 2, which also agrees with the theoretical prediction of the tearing-disruption scale $k_* = R_{m,\mathrm{eff}}^{4/7} \approx 1000$ (*9*–*12*), where $R_{m,\mathrm{eff}} = 2 \times 10^5$ is the $R_{m,\mathrm{eff}}$ due to the energy injection scale as the energy spectrum peaks at $k_\perp \approx 30$ [although Carbone *et al.* (*28*) predicted the same critical scale, $k_* = R_{m,\mathrm{eff}}^{4/7}$, as the first analytic study on this topic, it was derived on the basis of an incorrect model of MHD turbulence (*29*)]. For comparison, we ran another 3D simulation with a relatively low R_m (= 8×10^4) while keeping the initial condition identical. In this lower R_m simulation, we observed that flux ropes are essentially absent (see fig. S1), which corroborates the lack of any imprint from reconnection-driven cascades in the corresponding energy spectrum (the blue curves in Fig. 2). We, therefore, conclude that a sufficiently large R_m (> 10^5) is one of the prerequisites for evolving current sheets to become tearing-unstable in a turbulent bath, consequently leading to the copious formation of flux ropes before reaching the scale given by k_η.

We further investigate changes in the shape (i.e., anisotropy) of statistical eddies in the subinertial range, one key element in making reconnection-driven energy cascade dominate over energy cascade through MHD wave interactions. In the top panels of Fig. 3, we report the dependence of the half-width ξ (Fig. 3A) and aspect ratio ξ/λ (Fig. 3B) of the statistical eddies on the half-thickness λ based on second-order structure functions (see the "Shell-to-shell energy transfers in the inertial and tearing-mediated subinertial ranges" section). While the scaling $\xi/\lambda \propto \lambda^{-0.2}$ is observed in the traditional inertial range, in the subinertial range, the scaling changes to approximately $\xi/\lambda \propto \lambda^{-0.1}$. The scaling is in contrast to the previous theoretical prediction $\xi/\lambda \propto \lambda^{4/5}$ (*11*). Similarly, the bottom panels of Fig. 3 depict the relation between the half-length $\ell_\parallel$ and the half-thickness λ. A scaling relation $\ell_\parallel \propto \lambda^{1/2}$ is observed in the inertial range as expected from the theory. However, the scaling in the subinertial range, $\ell_\parallel \propto \lambda^{2/3}$ (and $\ell_\parallel/\lambda \propto \lambda^{-1/3}$), again deviates from the theoretical estimates (*11*). The theoretical predictions $\xi/\lambda \propto \lambda^{4/5}$ and $\ell_\parallel/\lambda \propto \lambda^{1/5}$ in the subinertial range require the assumption $\theta_t \sim \delta/\zeta$, where θ_t is the alignment angle, and δ and ζ denote the inner layer width and the wavelength of the fastest growing tearing mode, respectively (*11*). The difference between the theoretical predictions and the numerical experiments indicates that the assumption $\theta_t \sim \delta/\zeta$ needs further examination.

To address the underlying cause leading to this new range of the turbulent energy cascade, we also investigate the difference in the energy transfer between the inertial and subinertial ranges. For this purpose, we calculate the cylindrical shell-to-shell magnetic energy transfer function, $T_{bb}(Q, K) = -\int \mathbf{B}_K \cdot (\mathbf{u} \cdot \nabla)\mathbf{B}_Q \mathrm{d}^3x$, where $\mathbf{B}_K$ contains all Fourier modes $\tilde{\mathbf{B}}(\mathbf{k})$ in the Kth perpendicular wave number shell, $k_K < k_\perp < k_{K+1}$, and K is an integral shell number; $\mathbf{B}_Q(\mathbf{x})$ is defined in the same way for the Qth shell (see Materials and Methods for a detailed description). The red pixels in Fig. 4A represent positive magnetic energy transfer from the Qth shell to the Kth shell, and the blue pixels denote the opposite.

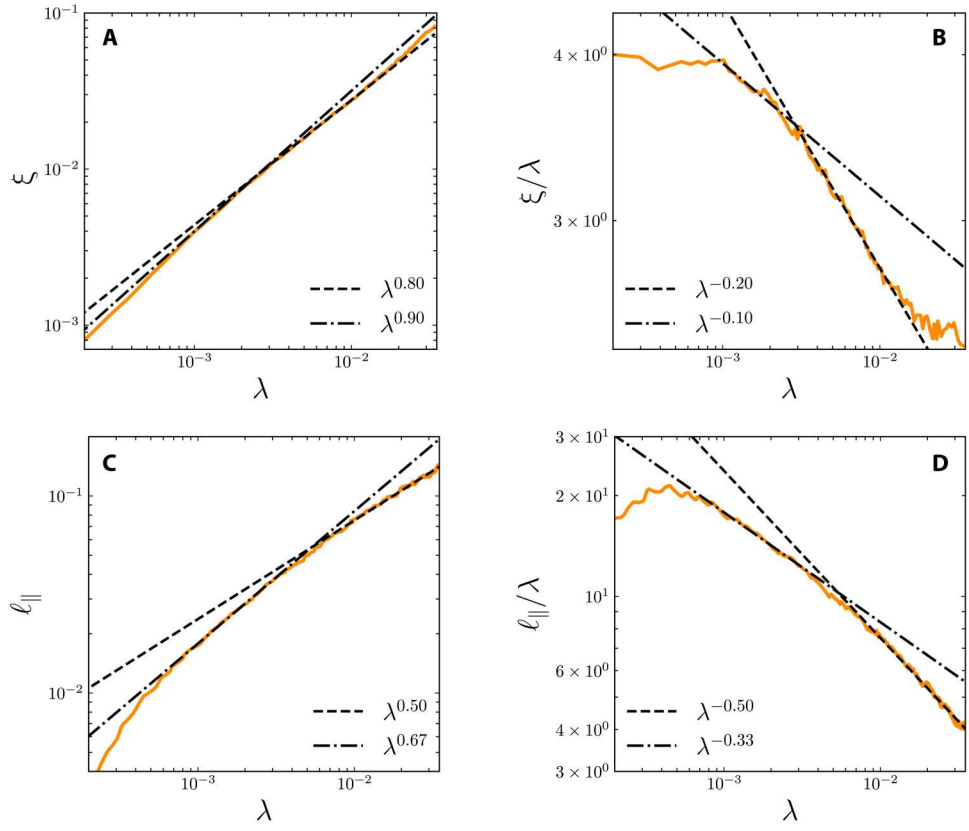

Fig. 3. Scale-dependent anisotropy of statistical eddies. (**A**) The perpendicular half-width ξ of the statistical eddies as a function of the perpendicular half-thickness λ. This function is obtained by equating the second-order **B**-trace structure function measured along ξ = 0 and λ = 0 axes in the ξ − λ plane. (**B**) Aspect ratio ξ/λ of the statistical eddies as a function of λ. (**C**) and (**D**) are the scaling relation between the parallel half-length $\ell_\parallel$ and λ, obtained in a similar way but in the local coordinate plane ξ = 0. The fitted dashed and dot-dashed lines show two scaling laws in the traditional inertial range and the tearing-mediated subinertial range of the turbulent energy cascade.

The diagonal pixels are white (i.e., empty) since there is no self-magnetic energy transfer by construction. The T_{bb} distribution on the k_Q-k_K phase plane in Fig. 4A is characterized by the main features such as local, forward transfer. Figure 4 (B and C) represents vertical cuts of T_{bb} normalized to

$$N_{\text{inertial}} \sim \frac{E_Q}{\tau_A}(k_Q L)^{-1/4} \sim \frac{E_Q^{3/2} k_Q}{(\rho V)^{1/2}}(k_Q L)^{-1/4} \quad (1)$$

and

$$N_{\text{tearing}} \sim \gamma_p E_Q \sim \frac{\eta^{1/2}}{(\rho V)^{1/4}} E_Q^{5/4} k_Q^{3/2} \quad (2)$$

where τ_A is the Alfvénic time scale and γ_p the linear growth rate of the tearing instability (see Materials and Methods for details). The factor $(k_Q L)^{-1/4}$ in Eq. 1 takes into account the reduction of nonlinearity due to dynamic alignment (*27*). Within the inertial range, energy transfer is expected to be self-similar, i.e., the energy transfer from the *Q*th shell to the *K*th shell operates in the same way as the transfer from the $(Q + 1)$th shell to the $(K + 1)$th shell. This is consistent with the observation in Fig. 4B that, when normalized to N_{inertial}, the three cuts in the inertial range (Fig. 4A, solid lines) strongly overlap. In contrast, the three cuts in the tearing-mediated range (Fig. 4A, dotted curves) do not exhibit self-similarity in Fig. 4B because of the underlying mechanism being different than the classical, inertial-range energy cascade. However, when T_{bb} is normalized by N_{tearing}, i.e., $T_{bb}/N_{\text{tearing}}$, the cuts in the tearing-mediated range (dashed curve) become self-similar (Fig. 4C), thus confirming the existence of a subinertial range within which the energy transfer is controlled by the tearing instability in reconnecting current sheets.

DISCUSSION

The present study suggests that the energy transfer in, e.g., the solar atmosphere at small scales can be fundamentally different from the classic paradigm of the turbulent energy cascade controlled by MHD wave interactions. Our calculated magnetic energy spectrum captures a new range of reconnection-driven energy cascade with a spectral index of −2.2. It is interesting to point out that the line-of-sight magnetic field observations of a coronal hole using magnetograms acquired by the Near-Infrared Imaging Spectrapolarimeter (NIRIS) operating at the Goode Solar Telescope of the Big Bear Solar Observatory showed that the turbulent magnetic energy spectra also exhibit a new range with a spectral index of −2.2 (*7*) (also see fig. S2), but it requires further observations to rule out the coincidence and then to identify the underlying mechanism that leads to the spectral break. On the other hand, similar

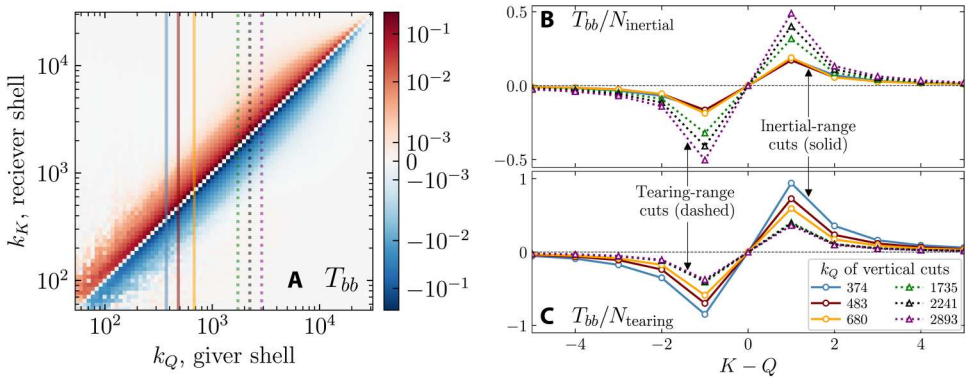

Fig. 4. Self-similarity of normalized cylindrical shell-to-shell energy transfers. (**A**) Magnetic-to-magnetic energy transfer functions $T_{bb}(Q, K) = -\int \mathbf{B}_K \cdot (u \cdot \nabla)\mathbf{B}_Q d^3x$ in the k_Q-k_K plane. (**B** and **C**) Normalized energy transfer function values along different vertical cuts in specific giver k_Q shells. The cut locations are marked in (A), with solid-line cuts chosen in the inertial range and dotted-line cuts in the reconnection-driven (or tearing-mediated) subinertial range. The normalization used in (B) and (C), $N_{\text{inertial}} = E_Q^{3/2}\, k_Q (k_Q L)^{-1/4}/(\rho V)^{1/2}$ and $N_{\text{tearing}} = \eta^{1/2} E_Q^{5/4} k_Q^{3/2}/(\rho V)^{1/4}$ (see Materials and Methods), is appropriate for the inertial range and the tearing-mediated subinertial range, respectively. The horizontal coordinates in (B) and (C) are the shell number differences (integers), $K - Q$.

observations acquired by the Helioseismic and Magnetic Imager (HMI) onboard the Solar Dynamic Observatory with a relatively low spatial resolution did not present a steepening in the corresponding energy spectra, suggesting that a high spatial resolution might be required to reveal this new range of energy transfer in the turbulent solar atmosphere. To address the discrepancy between the observations of NIRIS and HMI, we illustrated, with the same dataset in fig. S2, that the spatial resolution of observation can significantly influence the scientific findings.

In addition, spacecraft such as Solar Orbiter may also be able to reveal this newly identified subinertial range in magnetic energy spectra through remote sensing observations. Recently, Extreme Ultraviolet Imager (EUI) onboard Solar Orbiter observed transient small-scale brightenings prevalent in the corona of the quiet Sun termed "campfires" (*30*). It has been proposed that most campfire events observed by EUI are driven by magnetic reconnection, which may play an important role in the coronal heating of the quiet Sun (*31*, *32*). Our 3D simulation results in the large-R_m regime suggest that magnetic reconnection is a ubiquitous process in the turbulent solar corona where the R_m is even larger, and thus, the current sheets can thin down to much smaller scales and form the fractal structures within which copious formation of plasmoids occurs. Hence, there should be many more reconnection sites than observed, which can be revealed by (future) high-resolution extreme ultraviolet images.

In addition to the solar coronal heating (*30*, *31*), the omnipresence of plasmoids associated with magnetic reconnection, identified in this study, also has broad implications and consequences on particle acceleration in the solar/stellar coronae, accretion disks, and jets from compact objects (*33*, *34*), and on filament formation in the Herschel maps of the Orion A giant molecular cloud (*35*). Moreover, the ubiquitous presence of dense plasmoids in the interstellar medium can also play an important role in pulsar scintillation (*36*). All the aforementioned astrophysical systems are associated with large R_m ($> 10^5$) and thus could be characterized by the tearing-mediated turbulence identified in the present work.

MATERIALS AND METHODS

Model description

Following procedures previously described in (*24*), the governing equations of our numerical model are the dimensionless viscoresistive MHD equations

$$\partial_t \rho + \nabla \cdot (\rho \mathbf{u}) = 0 \tag{3}$$

$$\partial_t (\rho \mathbf{u}) + \nabla \cdot (\rho \mathbf{u}\mathbf{u}) = -\nabla (p + B^2/2) + \nabla \cdot (\mathbf{B}\mathbf{B}) + \nu \nabla^2 (\rho \mathbf{u}) \tag{4}$$

$$\partial_t p + \nabla \cdot (p \mathbf{u}) = (\gamma - 1)(-p \nabla \cdot \mathbf{u} + , \eta J^2), \tag{5}$$

$$\partial_t \mathbf{B} = \nabla \times (\mathbf{u} \times \mathbf{B} - \eta \mathbf{J}) \tag{6}$$

where ρ, $\mathbf{u}$, and p are the mass density, velocity, and pressure of the plasma, respectively; $\mathbf{B}$ is the magnetic field; and $\mathbf{J} = \nabla \times \mathbf{B}$ denotes the electric current density. The kinematic viscosity and the magnetic diffusivity are denoted as ν and η, respectively, while γ is the adiabatic index.

Model setup

We solve Eqs. 3 to 6 using the BATS-R-US MHD code (*37*) by adopting a fifth-order scheme (*38*) in a domain $[(x, y, z) : -L_0/2 \le x, y \le L_0/2, -L_0 \le z \le L_0]$, where L_0 is set to unity. Periodic boundary conditions are used in all three directions. Lengths are normalized to the box size L_0, velocities are normalized to the characteristic Alfvén speed V_A, and time is normalized to L_0/V_A. We initialize the simulations by placing uncorrelated, equipartitioned velocity and

magnetic field fluctuations in Fourier harmonics as follows

$$\psi = \sum_{l,m,n}(a_{mn}/2\pi)\sin(2\pi mx/L_x + 2\pi ny/L_y + 2\pi lz/L_z + \phi_{lmn}) \quad (7)$$

$$B_x = \frac{\partial\psi}{\partial y} = \sum_{l,m,n} a_{mn}(n/L_y)\cos(2\pi mx/L_x + 2\pi ny/L_y + 2\pi lz/L_z + \phi_{lmn}) \quad (8)$$

$$B_y = -\frac{\partial\psi}{\partial x} = -\sum_{l,m,n} a_{mn}(m/L_x)\cos(2\pi mx/L_x + 2\pi ny/L_y + 2\pi lz/L_z + \phi_{lmn}) \quad (9)$$

$$B_z = B_{z0} \quad (10)$$

where we set

$$a_{mn} = \frac{\sqrt{2}B_0}{N^{1/2}(m^2/L_x^2 + n^2/L_y^2)^{1/2}} \quad (11)$$

and $L_x = L_y = L_0$, and $L_z = 2L_0$. ϕ_{lmn} denotes random phases for each mode. The summation is over the range $0 \le m \le m_{max}$, $-n_{max} \le n \le n_{max}$. However, for $m = 0$, we limit the range to $0 < n < n_{max}$. The range of l is always $-l_{max} \le l \le l_{max}$. The total number of modes are

$$N = (2l_{max} + 1)[(2m_{max} + 1)(2n_{max} + 1) - 1]/2 \quad (12)$$

We only sum over half of the Fourier space because the (m, n) mode and the $(-m, -n)$ mode are not independent. Here, we choose $m_{max} = n_{max} = 10$ and $l_{max} = 5$. The above setup leads to

$$\langle B_\perp^2 \rangle = B_0^2 \quad (13)$$

where $\langle ... \rangle$ represents the spatial average.

For the velocity **u**, we use the similar expressions

$$u_x = \sum_{l,m,n} b_{mn}(n/L_y)\cos(2\pi mx/L_x + 2\pi ny/L_y + 2\pi lz/L_z + \phi'_{lmn}) \quad (14)$$

$$u_y = -\sum_{l,m,n} b_{mn}(m/L_x)\cos(2\pi mx/L_x + 2\pi ny/L_y + 2\pi lz/L_z + \phi'_{lmn}) \quad (15)$$

$$u_z = 0 \quad (16)$$

where we set

$$b_{mn} = \frac{\sqrt{2}u_0}{N^{1/2}(m^2/L_x^2 + n^2/L_y^2)^{1/2}} \quad (17)$$

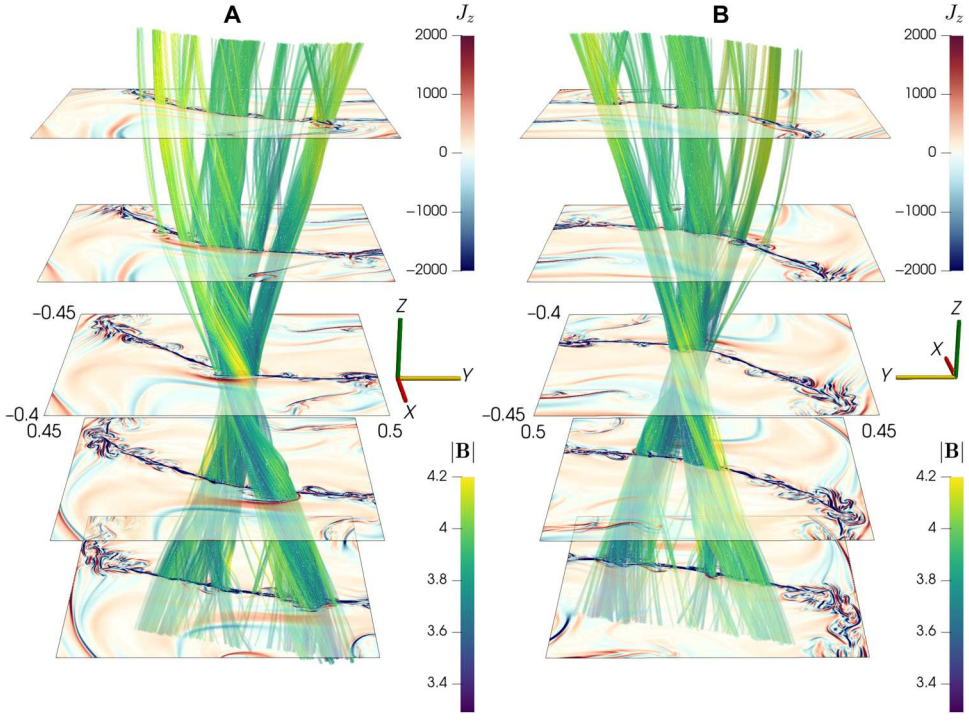

Fig. 5. 3D magnetic flux ropes with elongated current sheets. Flux ropes passing through a plasmoid located near the center of the current sheet are displayed in the intermediate 2D slice. The chosen views are along the $+x$ (**A**) and $-x$ (**B**) directions, respectively. Magnetic field lines are colored accordingly to the magnetic field magnitude $|\mathbf{B}|$, while the different x-y slices are colored by the value of the electric current density component, J_z, in the direction of the mean magnetic field.

Similarly, we have

$$\langle u_\perp^2 \rangle = u_0^2 \tag{18}$$

The plasma density and pressure are initially set to constant values $\rho = 1.0$ and $p = 1.6$, respectively. The constants B_0 and u_0 determine the strength of the initial velocity and magnetic field fluctuations. In this work, we set $B_0 = u_0 = 1$, which gives the initial turbulent energy $E = \langle u_\perp^2 + B_\perp^2 \rangle/2 = (u_0^2 + B_0^2)/2 = 1$. The mean magnetic field $B_{z0} = 4$ leads to a plasma beta (ratio of the plasma pressure to the magnetic pressure) $\beta \approx 0.2$. In the main 3D simulation presented here, the $R_m = u_0 L_0/\eta = 10^6$, where $\eta = 10^{-6}$ denotes the magnetic diffusivity. The $R_{m,\mathrm{eff}} = 2 \times 10^5$ due to the energy injection scale as the energy spectrum peaks at $k_\perp \approx 30$ (see Fig. 2). We set the viscosity $\nu = 10^{-6}$ such that the magnetic Prandtl number $P_m = \nu/\eta = 1$. This large R_m value allows the copious formation of flux ropes within the current sheets, as verified by visual inspection of the simulation data in a tiny subdomain (see example in Fig. 5). For the 2D simulations, we adopt similar initial setups but ignore the third dimension in z. For both 3D and 2D studies, we also ran one additional simulation with $R_m = 8 \times 10^4$ and a periodic box of ~2000 × 2000 × 1000 and ~2000 × 2000 grid cells, respectively (see fig. S1). Compared with the main 3D simulation (at a cost of about 200 million CPU hours with approximately 0.5 trillion grid cells), the computational cost of the rest simulations is negligible.

Second-order structure function

The anisotropy of statistical eddies shown in Fig. 3 is calculated on the basis of a second-order **B**-trace structure function. To calculate this structure function, we randomly sample a large number of data-point pairs. For each pair of points, 1 and 2, the displacement $\delta\mathbf{r} = \mathbf{r}_1 - \mathbf{r}_2$ is projected onto a local, scale-dependent coordinate system ($\ell_\parallel$, ξ, λ): $\ell_\parallel$ is along the local mean field $\mathbf{B}_{\mathrm{local}} = (\mathbf{B}_1 + \mathbf{B}_2)/2$, ξ is along the local perpendicular fluctuation field $\delta\mathbf{B}_{\perp,\mathrm{local}} = \mathbf{B}_{\mathrm{local}} \times [(\mathbf{B}_1 - \mathbf{B}_2) \times \mathbf{B}_{\mathrm{local}}]/|\mathbf{B}_{\mathrm{local}}|^2$, and λ completes the right-handed coordinate system. We then accumulate the contributions from all sampling pairs to compute the **B**-trace structure function $S_2 = \langle |\mathbf{B}_1 - \mathbf{B}_2|^2 \rangle$, an ensemble-averaged function of ($\ell_\parallel$, ξ, λ). As an example, here we show the cross section of S_2 in the $\ell_\parallel = 0$ plane. The consequent perpendicular structure function $S_{2\perp}$(ξ, λ) is illustrated in Fig. 6A, which exhibits clear anisotropy between the perpendicular half-width, ξ, of the statistical eddies and the perpendicular half-thickness, λ. It is immediately observed that Fig. 6A also depicts the perpendicular cross section of statistical eddies at different scales.

To further quantify the anisotropy, we investigate the aspect ratio of the perpendicular eddies, ξ/λ. To this end, we measure $S_{2\perp}$ along the two perpendicular axes, $S_{2\perp}(\xi; \lambda = 0)$ and $S_{2\perp}(\lambda; \xi = 0)$, as shown in Fig. 6B, and then find a mapping between ξ and λ by equating $S_{2\perp}$ along the two curves. This gives the result illustrated in Fig. 3. Following a similar procedure, we also obtain the relation between the parallel half-length, $\ell_\parallel$, and the perpendicular half-thickness, λ, in Fig. 3 based on the structure function S_2 in the ξ = 0 plane.

Shell-to-shell energy transfers in the inertial and tearing-mediated subinertial ranges

To further investigate the role of tearing instability in the turbulent energy cascade, we calculated the cylindrical shell-to-shell magnetic energy transfer function (*39*)

$$T_{bb}(Q, K) = -\int \mathbf{B}_K \cdot (\mathbf{u} \cdot \nabla)\, \mathbf{B}_Q \mathrm{d}^3 x \tag{19}$$

Here,

$$\mathbf{B}_K(\mathbf{x}) = \int_{k_K < k_\perp < k_{K+1}} \widetilde{\mathbf{B}}(\mathbf{k}) e^{i\mathbf{k}\cdot\mathbf{x}} \mathrm{d}^3 k \tag{20}$$

contains all Fourier modes $\widetilde{\mathbf{B}}(\mathbf{k})$ in the Kth perpendicular wave number shell, $k_K < k_\perp < k_{K+1}$, and K is an integral shell number. $\mathbf{B}_Q(\mathbf{x})$ is defined in the same way for the Qth shell. $T_{bb}(Q, K)$ then gives the transfer rate of magnetic energy from the Qth shell to the Kth shell (*40*, *41*) or, correspondingly, from the spatial scale $\sim 1/k_Q$ to the scale $\sim 1/k_K$. We adopted 100 logarithmic bins along the K and Q directions between $k_\perp = 2\pi$ and $k_\perp = 10^4\pi$. The resulting T_{bb} values from our simulation on the k_Q-k_K plane is shown in Fig. 4A. The dominance of red pixels above the diagonal where $k_K > k_Q$ confirms the forward transfer from larger to smaller scales. Figure 4A also shows that transfers occur primarily close to the diagonal, indicating that the energy transfer is mostly local.

Normalization of the cylindrical shell-to-shell energy transfer rate

In the inertial range, we assume that Boldyrev's turbulence theory with dynamic alignment holds (*27*). In this picture, turbulence eddies are anisotropic in all three directions, with dimensions ξ

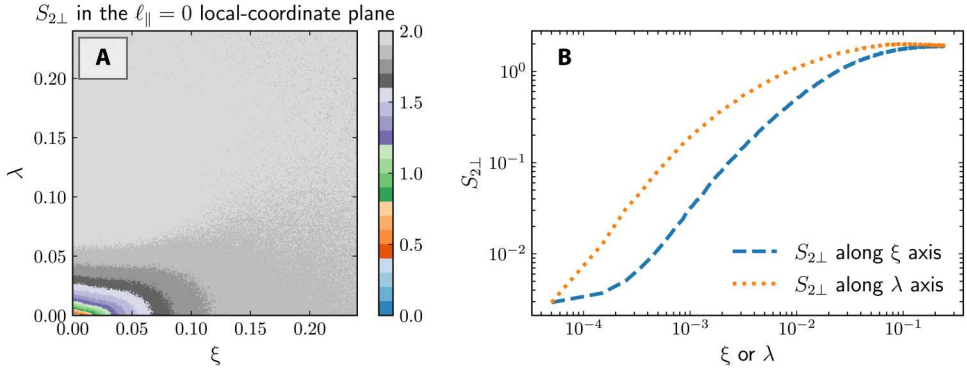

Fig. 6. Anisotropy of the statistical eddies perpendicular to the local mean magnetic field. (**A**) Cross sections of the statistical eddies at different values from the second-order structure function $S_{2\perp} = \langle |\mathbf{B}_1 - \mathbf{B}_2|^2 \rangle$. (**B**) $S_{2\perp}$ as a function of the perpendicular half-width ξ or the perpendicular half-thickness λ of the statistical eddies.

and λ perpendicular to the local field and $\ell_\parallel$ along the local field. These scales are related as $\xi \sim L(\lambda/L)^{3/4}$ and $\ell_\parallel \sim L(\lambda/L)^{1/2}$, where L is the large-scale length. The magnetic fluctuation $B_\lambda \sim B_0(\lambda/L)^{1/4}$ at scale λ, where B_0 is the large-scale magnetic field. The energy cascade of eddies at scale λ occurs on the time scale $\tau_\lambda \sim \ell_\parallel/V_{A0} \sim \xi/V_{A\lambda}$. Let E_Q be the magnetic energy in the Qth shell (i.e., the perpendicular wave number $k_\perp$ satisfies $k_Q < k_\perp < k_{Q+1}$) and V be the volume of the domain. The magnetic energy density E_Q/V on the $\lambda_Q \sim 1/k_Q$ scale is proportional to $B_Q^2/2$; therefore, the Alfvén speed $V_{AQ} = B_Q/\sqrt{\rho} \sim E_Q^{1/2}/(V\rho)^{1/2}$ and the cascade time $\tau_Q \sim \xi_Q/V_{AQ} \sim (k_QL)^{1/4}(V\rho)^{1/2}/E_Q^{1/2}k_Q$. This leads to the normalization $N_{\text{inertial}} \sim E_Q/\tau_Q \sim (k_QL)^{-1/4}E_Q^{3/2}k_Q/(\rho V)^{1/2}$. We expect $T_{bb}(Q, K)/N_{\text{inertial}}$ in Fig. 4B to be approximately independent of Q in the inertial range.

In the tearing-mediated range, the energy cascade time is governed by $1/\gamma_p$, where γ_p is the linear growth rate of the tearing instability. For a current sheet with a half-thickness λ and an upstream Alfvén speed $V_{A\lambda}$, the linear growth rate (*42*) $\gamma_p \sim (V_{A\lambda}\lambda/\eta)^{-1/2}V_{A\lambda}/\lambda$. For the Qth shell, $\lambda \sim 1/k_Q$, $V_{A\lambda} \sim E_Q^{1/2}/(V\rho)^{1/2}$. Hence, we propose another normalization for the reconnection-driven (or tearing-mediated) subinertial range, $N_{\text{tearing}} \sim \gamma_p E_Q \sim \eta^{1/2}E_Q^{5/4}k_Q^{3/2}/(\rho V)^{1/4}$. We expect $T_{bb}(Q, K)/N_{\text{tearing}}$ in Fig. 4C to be nearly independent of Q in the tearing-mediated subinertial range.

In our simulation, the plasma density $\rho \simeq 1$ and the volume $V = 2$. We adopt the value $\rho V = 2$ in the normalization for producing Fig. 4.

Supplementary Materials

This PDF file includes:
Sections S1 and S2
Figs. S1 and S2

Other Supplementary Material for this manuscript includes the following:
Movie S1

REFERENCES AND NOTES

1. P. S. Iroshnikov, Turbulence of a conducting fluid in a strong magnetic field. *Astronomicheskii Zhurnal* **40**, 742 (1963).
2. R. H. Kraichnan, Inertial-range spectrum of hydromagnetic turbulence. *Phys. Fluids* **8**, 1385 (1965).
3. P. Goldreich, S. Sridhar, Toward a theory of interstellar turbulence. II. Strong alfvenic turbulence. *Astrophys. J.* **438**, 763 (1995).
4. W. H. Matthaeus, S. L. Lamkin, Turbulent magnetic reconnection. *Phys. Fluids* **29**, 2513 (1986).
5. D. Biskamp, H. Welter, Dynamics of decaying two-dimensional magnetohydrodynamic turbulence. *Physics of Fluids B: Plasma Physics* **1**, 1964–1979 (1989).
6. K. H. Kiyani, K. T. Osman, S. C. Chapman, Dissipation and heating in solar wind turbulence: From the macro to the micro and back again. *Philos. Trans. R. Soc. Lond. A* **373**, 20140155 (2015).
7. V. I. Abramenko, V. B. Yurchyshyn, Analysis of quiet-sun turbulence on the basis of SDO/HMI and goode solar telescope data. *Mon. Notices Royal Astron. Soc.* **497**, 5405–5412 (2020).
8. R. Kieokaew, B. Lavraud, Y. Yang, W. H. Matthaeus, D. Ruffolo, J. E. Stawarz, S. Aizawa, C. Foullon, V. Génot, R. F. Pinto, N. Fargette, P. Louarn, A. Rouillard, A. Fedorov, E. Penou, C. J. Owen, T. S. Horbury, H. O'Brien, V. Evans, V. Angelini, Solar Orbiter observations of the Kelvin-Helmholtz waves in the solar wind. *Astron. Astrophys.* 656, A12 (2021).
9. N. F. Loureiro, S. Boldyrev, Role of magnetic reconnection in magnetohydrodynamic turbulence. *Phys. Rev. Lett.* **118**, 245101 (2017).
10. A. Mallet, A. A. Schekochihin, B. D. G. Chandran, Disruption of sheet-like structures in alfvénic turbulence by magnetic reconnection. *Mon. Notices Royal Astron. Soc.* **468**, 4862–4871 (2017).
11. S. Boldyrev, N. F. Loureiro, Magnetohydrodynamic turbulence mediated by reconnection. *Astrophys. J.* **844**, 125 (2017).
12. L. Comisso, Y.-M. Huang, M. Lingam, E. Hirvijoki, A. Bhattacharjee, Magnetohydrodynamic turbulence in the plasmoid-mediated regime. *Astrophys. J.* **854**, 103 (2018).
13. N. F. Loureiro, S. Boldyrev, Nonlinear reconnection in magnetized turbulence. *Astrophys. J.* **890**, 55 (2020).
14. N. F. Loureiro, A. A. Schekochihin, S. C. Cowley, Instability of current sheets and formation of plasmoid chains. *Phys. Plasmas* **14**, 100703 (2007).
15. F. Pucci, M. Velli, Reconnection of quasi-singular current sheets: The "ideal" tearing mode. *Astrophys. J. Lett.* **780**, L19 (2014).
16. L. Comisso, M. Lingam, Y. M. Huang, A. Bhattacharjee, General theory of the plasmoid instability. *Phys. Plasmas* **23**, 100702 (2016).
17. D. A. Uzdensky, N. F. Loureiro, Magnetic reconnection onset via disruption of a forming current sheet by the tearing instability. *Phys. Rev. Lett.* **116**, 105003 (2016).
18. Y.-M. Huang, L. Comisso, A. Bhattacharjee, Plasmoid instability in evolving current sheets and onset of fast reconnection. *Astrophys. J.* **849**, 75 (2017).
19. A. Lazarian, G. L. Eyink, A. Jafari, G. Kowal, H. Li, S. Xu, E. T. Vishniac, 3D turbulent reconnection: Theory, tests, and astrophysical implications. *Phys. Plasmas* **27**, 012305 (2020).
20. A. A. Schekochihin, MHD turbulence: A biased review. *J. Plasma Phys.* **88**, 155880501 (2022).
21. D. Biskamp, *Magnetohydrodynamic Turbulence* (Cambridge Univ. Press, 2003).
22. W. Daughton, V. Roytershteyn, H. Karimabadi, L. Yin, B. J. Albright, B. Bergen, K. J. Bowers, Role of electron physics in the development of turbulent magnetic reconnection in collisionless plasmas. *Nat. Phys.* **7**, 539–542 (2011).
23. Y.-M. Huang, A. Bhattacharjee, Turbulent magnetohydrodynamic reconnection mediated by the plasmoid instability. *Astrophys. J.* **818**, 20 (2016).
24. C. Dong, L. Wang, Y.-M. Huang, L. Comisso, A. Bhattacharjee, Role of the plasmoid instability in magnetohydrodynamic turbulence. *Phys. Rev. Lett.* **121**, 165101 (2018).
25. T. Li, E. Priest, R. Guo, Three-dimensional magnetic reconnection in astrophysical plasmas. *Proc. R. Soc. A* **477**, 20200949 (2021).
26. O. Pezzi, F. Pecora, J. Le Roux, N. Engelbrecht, A. Greco, S. Servidio, H. Malova, O. Khabarova, O. Malandraki, R. Bruno, O. Pezzi, S. Servidio, G. Li, W. Matthaeus, J. Le Roux, N. E. Engelbrecht, F. Pecora, L. Zelenyi, V. Obridko, V. Kuznetsov, Current sheets, plasmoids and flux ropes in the heliosphere. *Space Sci. Rev.* **217**, 38 (2021).
27. S. Boldyrev, Spectrum of magnetohydrodynamic turbulence. *Phys. Rev. Lett.* **96**, –115002 (2006).
28. V. Carbone, P. Veltri, A. Mangeney, Coherent structure formation and magnetic field line reconnection in magnetohydrodynamic turbulence. *Phys. Fluids A* **2**, 1487–1496 (1990).
29. S. Boldyrev, N. F. Loureiro, Tearing instability in Alfvén and Kinetic-Alfvén turbulence. *J. Geophys. Res.* **125**, e28185 (2020).
30. D. Berghmans, F. Auchère, D. M. Long, E. Soubrié, M. Mierla, A. N. Zhukov, U. Schühle, P. Antolin, L. Harra, S. Parenti, O. Podladchikova, R. Aznar Cuadrado, É. Buchlin, L. Dolla, C. Verbeeck, S. Gissot, L. Teriaca, M. Haberreiter, A. C. Katsiyannis, L. Rodriguez, E. Kraaikamp, P. J. Smith, K. Stegen, P. Rochus, J. P. Halain, L. Jacques, W. T. Thompson, B. Inhester, Extreme-UV quiet sun brightenings observed by the Solar Orbiter/EUI. *Astron. Astrophys.* **656**, L4 (2021).
31. Y. Chen, D. Przybylski, H. Peter, H. Tian, F. Auchère, D. Berghmans, Transient small-scale brightenings in the quiet solar corona: A model for campfires observed with Solar Orbiter. *Astron. Astrophys.* **656**, L7 (2021).
32. D. Clery, 'Campfires' may drive heating of solar atmosphere. *Science* **372**, 557–558 (2021).
33. J. F. Drake, M. Swisdak, H. Che, M. A. Shay, Electron acceleration from contracting magnetic islands during reconnection. *Nature* **443**, 553–556 (2006).
34. L. Comisso, L. Sironi, Ion and electron acceleration in fully kinetic plasma turbulence. *Astrophys. J. Lett.* **936**, L27 (2022).
35. S. Kong, V. Ossenkopf-Okada, H. G. Arce, J. Bally, Á. Sánchez-Monge, P. McGehee, S. Suri, R. S. Klessen, J. M. Carpenter, D. C. Lis, F. Nakamura, P. Schilke, R. J. Smith, S. Mairs, A. Goodman, M. J. Maureira, The CARMA-NRO Orion Survey: Filament formation via collision-induced magnetic reconnection—The stick in Orion A. *Astrophys. J.* **906**, 80 (2021).
36. R. Narayan, The physics of pulsar scintillation. *Philos. Trans. R. Soc. Lond. A* **341**, 151–165 (1992).
37. G. Tóth, B. van der Holst, I. V. Sokolov, D. L. De Zeeuw, T. I. Gombosi, F. Fang, W. B. Manchester, X. Meng, D. Najib, K. G. Powell, Q. F. Stout, A. Glocer, Y.-J. Ma, M. Opher, Adaptive numerical algorithms in space weather modeling. *J. Comput. Phys.* **231**, 870–903 (2012).
38. Y. Chen, G. Tóth, T. I. Gombosi, A fifth-order finite difference scheme for hyperbolic equations on block-adaptive curvilinear grids. *J. Comput. Phys.* **305**, 604–621 (2016).

39. A. Alexakis, B. Bigot, H. Politano, S. Galtier, Anisotropic fluxes and nonlocal interactions in magnetohydrodynamic turbulence. *Phys. Rev. E* **76**, 056313 (2007).
40. A. Alexakis, P. D. Mininni, A. Pouquet, Shell-to-shell energy transfer in magnetohydrodynamics. I. Steady state turbulence. *Phys. Rev. E* **72**, 046301 (2005).
41. O. Debliquy, M. K. Verma, D. Carati, Energy fluxes and shell-to-shell transfers in three-dimensional decaying magnetohydrodynamic turbulence. *Phys. Plasmas* **12**, 042309 (2005).
42. D. Biskamp, *Magnetic Reconnection in Plasmas*, vol. 3 (Cambridge Univ. Press, 2000).

Acknowledgments: We acknowledge fruitful discussions with M. Zhou, S. Cerri, N. Liu, M. Lingam, Y. Chen, G. Hammett, S. Cowley, and A. Burrows. Resources supporting this work were provided by the NASA High-End Computing (HEC) Program through the NASA Advanced Supercomputing (NAS) Division at Ames Research Center. We also would like to acknowledge high-performance computing support from Cheyenne (doi:10.5065/D6RX99HX) provided by NCAR's CISL, sponsored by NSF, and from National Energy Research Scientific Computing Center, a DOE Office of Science user facility. **Funding:** This work was partially supported by NASA grants 80NSSC19K0621 and 80NSSC21K1326, DOE grants DE-SC0021205 and DE-SC0021254, and DOE under contract number DE-AC02-09CH11466. **Author contributions:** All of the authors made notable contributions to this work. C.D. and Y.-M.H. designed the simulation for this study; C.D. carried out the simulations of MHD turbulence; C.D., L.W., Y.-M.H., L.C., and T.A.S. analyzed the simulation results; C.D., L.W., Y.-M.H., L.C., and A.B. wrote the paper; and all authors read the paper. **Competing interests:** The authors declare that they have no competing interests. **Data and materials availability:** All data needed to evaluate the conclusions in the paper are present in the paper and/or the Supplementary Materials.

Submitted 17 December 2021
Accepted 28 October 2022
Published 7 December 2022
10.1126/sciadv.abn7627